PONTIFICIA UNIVERSIDAD CATOLICA DE CHILE

ESCUELA DE INGENIERIA

EXTENSION OF DUPLEXED SINGLE-ENDED DISTRIBUTED TEMPERATURE SENSING CALIBRATION ALGORITHMS AND THEIR APPLICATION IN GEOTHERMAL SYSTEMS

MATÍAS LILLO BRICEÑO

Thesis submitted to the Office of Research and Graduate Studies in partial fulfillment of the requirements for the Degree of Master of Science in Engineering.

Advisor:

FRANCISCO SUÁREZ POCH

Santiago de Chile, April, 2022

PONTIFICIA UNIVERSIDAD CATOLICA DE CHILE

ESCUELA DE INGENIERIA

EXTENSION OF DUPLEXED SINGLE-ENDED DISTRIBUTED TEMPERATURE SENSING CALIBRATION ALGORITHMS AND THEIR APPLICATION IN GEOTHERMAL SYSTEMS

MATÍAS LILLO BRICEÑO

Members of the Committee:

FRANCISCO SUÁREZ
SARAH LERAY
MARK HAUSNER
GONZALO CORTAZAR

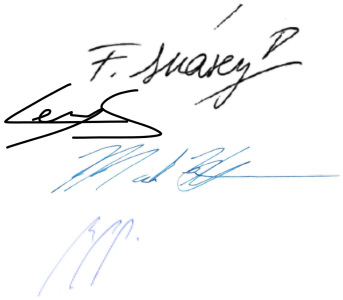

Thesis submitted to the Office of Research and Graduate Studies in partial fulfillment of the requirements for the Degree of Master of Science in Engineering.

Santiago de Chile, April, 2022

ACKNOWLEDGMENTS

I would like to thank my advisor Francisco Suárez for always encouraging me, teaching me, supporting my work and challenging me to go further, always with patience and good spirits. I also thank the people who at some point worked on the data collection that I used for my analysis; without their work my research would not have been possible.

Thanks to my family for supporting me on this long journey full of difficulties. Thanks to all my classmates, teachers and friends known during this stage of my life, who contributed to my academic and personal formation.

Thanks to the institutions that contributed to the development of my training and research: the Chilean National Research and Development Agency through project ANID/FONDECYT/1201354, the Centro de Desarrollo Urbano Sustentable (CEDEUS – ANID/FONDAP/15200001) and the Centro de Excelencia en Geotermia de los Andes (CEGA – ANID/FONDAP/15090013), as well as from the project ANID/FONDECYT/1210221. Also thanks to Andina Division of Codelco-Chile for provide the permission and logistic support in terms of personnel and mining well enabled to perform thermal observations.

CONTENTS

Page

LIST OF TABLES

LIST OF FIGURES

ABSTRACT

Fiber-optic distributed temperature sensing (DTS) has been widely used since the end of the 20th century, with various industrial, Earth sciences and research applications. To obtain precise thermal measurements, it is important to extend the currently available DTS calibration methods, considering that environmental and deployment factors can strongly impact the measurements. In this work, a laboratory experiment was performed to assess a currently available duplexed single-ended DTS calibration algorithm, and to extend it in case no temperature information is available at the end of the cables, which is extremely important in geothermal applications. The extended calibration algorithms were tested in different boreholes located in the Atacama Desert and in the Central Andes Mountains to estimate the geothermal gradient in these regions. The best algorithm found achieved a root mean square error of 0.31 ± 0.07 °C at the far end of a ~1.1 km cable, which is much smaller than that obtained using the manufacturer algorithm (2.17 ± 0.35 °C). Moreover, temperature differences between single- and double-ended measurements were less than 0.3 °C at the far end of the cable, which results in differences of ~0.5°C km^{-1} when determining the geothermal gradient. This improvement in the geothermal gradient is relevant, as it can reduce the drilling depth by at least 700 m in the study area. Future work should investigate new extensions of the algorithms for other DTS configurations and determining the flow rate of the Central Andes Mountains artesian well using the geothermal profile provided by the DTS measurements and the available data of the borehole.

RESUMEN

La detección de temperatura distribuida por fibra óptica (DTS por sus siglas en inglés) ha sido ampliamente utilizada desde finales del siglo 20, con varias aplicaciones industriales, en ciencias de la Tierra y aplicaciones de investigación. Para obtener mediciones térmicas precisas, es importante extender los métodos de calibración actualmente disponibles para DTS, considerando que factores medioambientales y de despliegue pueden impactar fuertemente a las mediciones. En este trabajo, se realizo un experimento de laboratorio para evaluar un algoritmo de calibración de DTS para configuraciones dúplex de un único extremo y extenderlo en caso de que no se disponga de información de temperatura al final del cable, lo cual es extremadamente importante en aplicaciones geotérmicas. Los algoritmos de calibración extendida se probaron en diferentes pozos ubicados en el Desierto de Atacama y en los Andes Centrales para estimar el gradiente geotérmico en estas regiones. El mejor algoritmo logró un error cuadrático medio de 0.31 ± 0.07 °C en el extremo lejano del cable a ~1.1 km, lo cual es mucho menor que el obtenido usando el algoritmo de (2.17 ± 0.35 °C). Además, las diferencias de temperatura entre mediciones de uno y dos extremos fueron inferiores a 0.3 ºC en el extremo lejano del cable, lo cual resulta en diferencias de ~0.5°C km^{-1} al determinar el gradiente geotermal. Esta mejora en el gradiente geotérmico es relevante ya que puede reducir la profundidad de perforación en al menos 700 m en el área de estudio. El trabajo futuro debería investigar nuevas extensiones de los algoritmos para otras configuraciones de DTS y determinar el flujo de agua del pozo artesiano en los Andes Centrales utilizando el perfil geotermal proporcionado por las mediciones DTS y la información disponible del sondaje.

1. Introduction

The determination of the geothermal gradient is relevant for many applications in a wide range of disciplines (Kutasov & Eppelbaum, 2009; Miranda et al., 2020). In renewable and sustainable energy sources, underground temperatures allow determining local and regional geothermal potential (Macenić et al., 2020), and the source temperature defines low- and high-enthalpy geothermal reservoirs (Miranda et al., 2020; Nian & Cheng, 2018). In Earth sciences, geothermal data are required to understand the dynamics of tectonic plates in ridge collision zones (Cande et al., 1987), to determine the effects of temperature in metamorphic formations (Iwamori, 2000), and for detecting re-initiation of volcanic activity (Muñoz & Hamza, 1993), among others (DiPietro, 2013; Gupta & Roy, 2007; Lowell et al., 2014). Obviously, actual temperature observations are also needed to develop detailed thermal models (Araya Vargas et al., 2021; Valdenegro et al., 2019). Moreover, borehole temperature profiles have been used to determine climate variations in different locations around the globe (Beltrami & Mareschal, 1992; Clauser & Mareschal, 1995; Pickler et al., 2018). The bottom hole temperature (BHT) method is the most common technique to record borehole temperatures and to use them to estimate the geothermal gradient (Barba et al., 2021; Dhia, 1987; Macenić et al., 2020). This technique is primarily used in the oil extraction industry where drilling is common and abundant data are available (Peters & Nelson, 2012). Borehole temperatures also can be used to predict static formation temperatures, thermophysical properties and production parameters in oil reservoirs (Liu et al., 2016), and to determine heat flow maps (Madon & Jong, 2021). However, measurements taken by the BHT method often have poor accuracy and corrections must be performed to improve these observations (Drury, 1984; Goutorbe et al., 2007). For instance, Goutorbe et al. (2007) show that most of the correction models leads to reliable estimation of temperature within ±10 °C. In thermal methods that are used to estimate geothermal gradients, direct temperature-depth relationships are determined and then correlated with properties of the geothermal system, being fairly simple to measure near-surface temperatures by airborne or satellite-based measurements

(Ovnatanov & Tamrazyan, 1970; Watson et al., 1990). However, as a near-surface method, they are limited to shallow depths (Domra Kana et al., 2015). For instance, according to Lv et al. (2018), the penetration depth determined using satellites could be of ~0.3 m, depending on soil properties and moisture. With their spatial and temporal coverage, Raman spectra fiber-optic distributed temperature sensing (DTS) methods offer significant advantages over traditional measurements systems in the environment (Sellwood et al., 2015; Suárez, Aravena, et al., 2011). DTS has been widely used as an in-situ logging technique in oil and gas wells, being the only system that offers a data profile that can be used to identify flow patterns, changes in fluid properties, and to monitor the overall integrity of the borehole without intervention (Williams et al., 2000). Since the 1990s, this technology has had various uses in geosciences (Förster et al., 1997; Hurtig et al., 1994), environmental sciences (Sayde et al., 2015; Suárez et al., 2020; Tyler et al., 2009; van Ramshorst et al., 2019), ecology (M. B. Hausner et al., 2013), glaciology (Tyler et al., 2013), hydrology (Lagos et al., 2020; Selker et al., 2006; Steele-Dunne et al., 2010), hydrogeology (Bense et al., 2016; Ghafoori et al., 2020; Lowry et al., 2007), engineering (Ruskowitz et al., 2014; Suárez et al., 2010), and industrial applications (Williams et al., 2000).

Although DTS systems have been successfully used in many environments, achieving high-resolution data is not trivial as their precision and accuracy depend on the prescribed spatial and temporal sampling intervals (Selker et al., 2006), deployment and configuration (e.g., single- or double-ended configurations), and calibration methodologies (Arnon et al., 2014; M. Hausner & Kobs, 2016; van de Giesen et al., 2012). Many practical issues can degrade the data quality, among which are the failure in connectors, splices, sharp bends and strains in the cable, excessive heat, and mechanical damage (Williams et al., 2000), which can be overcome by developing calibration algorithms (M. Hausner et al., 2011; M. Hausner & Kobs, 2016). Nonetheless, only few investigations have development these algorithms. Hausner et al. (2011) determined efficient ways to use the DTS Raman raw data to improve precision and accuracy of these systems in duplexed single-ended configurations. Hausner & Kobs (2016) developed an

approach to identify and correct step losses in single-ended configurations, whereas van de Giesen et al. (2012) developed a calibration algorithm for double-ended configurations using information from both ends of the optical fiber (see below for details about the different DTS configurations). Even when non-uniform differential attenuation can be addressed using double-ended configurations, in some situations only a single-ended configuration can be achieved. For instance, we performed a field campaign to determine the unexplored geothermal gradient in the central Andes of Chile, which is one of the countries with largest geothermal potential around the world that it is still unexploited (Morata, 2014; Suárez et al., 2014). Knowing the geothermal gradient in this region is relevant as it can be used for thermomechanical geological models; it serves as a baseline for geothermal exploitation; and at a broader scale it provides an extrapolation constraint for crustal/lithospheric rheology. Given logistical constraints during the field campaign, data were collected in a ~1.1 km long borehole using single-ended data with no independent thermal measurement at the bottom of the borehole. This issue did not allow obtaining an accurate temperature at the end of the borehole as different calibration algorithms cannot be fully constrained (M. Hausner et al., 2011), resulting in an uncertainty of more than 4 °C at the far end of the fiber-optic cable. This uncertainty may have important implications for data interpretation. The calibration algorithms developed so far for single-ended configurations assume a uniform differential along the fiber and consequently distributes the errors along the entire fiber (M. Hausner et al., 2011; M. Hausner & Kobs, 2016). Therefore, extending these algorithms to consider different differential attenuation rates and raising awareness of their existence is important for the scientific community that uses fiber optic DTS systems. We performed laboratory experiments to improve the accuracy and precision of single-ended DTS data by extending the current calibration algorithms, and then we applied these new algorithms to the geothermal data collected in different boreholes located in north and central Chile. The application of the extended algorithms improved the accuracy of the geothermal measurements in one order of magnitude, which reduced the uncertainty in drilling depth

by 50% when using DTS methods calibrated with the best algorithm that we found (compared to the BHT approach).

1.1. Hypothesis

The development of a calibration algorithm for duplexed single-ended configurations can result in temperatures with high precision, allowing to obtain differences of less than 0.1 ºC between a single- and a double-ended configuration for measurements in boreholes up to 1 km long and temperature differences of up to 0.3 ºC at the far end of the fiber optic cable compared to independent measurements, which can be used in applications such as the estimation of geothermal gradients.

1.2. Objectives

The main objective of this work is to assess and expand current duplexed single-ended configuration algorithms to reduce the uncertainty at the far-end of the fiber optic cable when no independent measurements of temperature are available in that point. Therefore, independent objectives are proposed.

1. Investigate the impact of the different physical parameters used in the calibration of the data on the temperatures obtained, including the effects of a step loss.
2. Perform a laboratory experiment with the same instrument and configuration used in the central Andean Chile to assess the accuracy of the calibration algorithms comparing independent temperature measurements at different distances.
3. Evaluate the current calibration algorithms and the proposed improvements in different Chilean Andean settings using the raw data collected by our team in the central Andean Chile and the raw data collected by Pickler et al. (2018) in boreholes of the northern Chile with a duplexed double-ended configuration.

4. Estimate the geothermal gradients using calibrated temperature data collected from boreholes located in different Chilean Andean settings and compare the results with results obtained by Pickler et al. (2018).

1.3. Thesis structure

The structure of the document is the following: Chapter 1 correspond to the introduction of the thesis, including the research objectives. Chapter 2 correspond to a description of the DTS theory, including the current and proposed calibration algorithms. Chapter 3 describes the materials and methods related to the experimental setups, measurement campaigns and metrics used for the evaluation of the algorithms. Chapter 4 shows the results of each evaluation, including the comparison between the different calibration algorithms and the resulting geothermal gradients in the different Chilean Andes setting considered. Chapter 5 present the main conclusions of the research. Finally, chapter 6 contain the references cited.

2. Raman spectra DTS theory

Raman spectra DTS technologies use optical fibers as distributed sensors than can be deployed for more than 40 km with a temperature resolution less than 1 °C (Dai et al., 2018; J. Li et al., 2019), or even shorter distances with correspondingly finer temperature (J. Li et al., 2019). Current DTS technologies allow a spatial sampling resolution on the order of centimeters (H. Li et al., 2021). The instruments used in this research have a minimum spatial integration of 0.25 and 1 m for fibers up to 1,000 m long, and a temporal integration as short as 2 and 10 seconds (Selker et al., 2006), although all these specifications cannot be obtained at the same time (Suárez, Aravena, et al., 2011). To estimate the thermal profile along a fiber-optic cable, a DTS instrument sends a laser pulse into the fiber and measures the backscattered Stokes and anti-Stokes intensities, which have information about the temperature at the location where the backscatter occurred. Then, optical time reflectometry is used to determine the position where backscatter

occurred (M. Hausner et al., 2011). Therefore, the temperature T(K) at position z (m) in the cable is expressed as (M. Hausner et al., 2011; Suárez, Aravena, et al., 2011):

$$T(z) = \frac{\gamma}{C + R(z) - \Delta\alpha\, z} \quad (1)$$

where γ (K) represents the shift in energy between a photon at the wavelength of the incident laser and the scattered Raman photon, C (-) is a calibration parameter that encompasses properties of the incident laser and the DTS instrument itself, $R(z) = ln(I_S(z)/I_{aS}(z))$ is the natural logarithm of the ratio between the Sokes and anti-Stokes signals, $I_S(z)$ and $I_{aS}(z)$, respectively, and $\Delta\alpha$ (m^{-1}) is the differential attenuation rate between the backscattered Stones and anti-Stokes signals. Since a detailed description of the DTS theory can be found elsewhere (M. Hausner et al., 2011; Suárez, Hausner, et al., 2011), below we describe the different DTS configurations, with emphasis on duplexed-single ended configurations and their current calibration algorithms, as well as to describe how these algorithms are extended and applied to determine the geothermal profile in different Chilean Andean settings..

2.1. DTS configurations and current calibration algorithms

There are three typical DTS configurations: simple single-ended, duplexed single-ended and duplexed double-ended configurations (M. Hausner et al., 2011) (Figure 1). The simple single-ended configuration uses only one connection to the DTS instrument, and the temperature is measured along the fiber from the DTS onwards. The duplexed single-ended configuration also uses only one connection to the DTS instrument, but there are two co-located fibers that measure temperature with two observations at every section along the cable. This configuration is made by deploying the cable in such a way that the fiber goes out from the DTS instrument and then comes back towards the instrument following the same path, without connecting the end of the cable into the instrument, or by using a cable with two co-located fibers spliced at the far end. The duplexed double-ended configuration is similar to the duplexed single-ended configuration, but with both of the co-located fibers connected to the DTS instrument, and the instrument measuring

from alternating ends of the fiber. Thus, temperature observations are performed from both directions within the fiber.

Many DTS instruments have proprietary algorithms provided by the manufacturers that use some form of equation (1) to calibrate the thermal profile along the cable (also known as the temperature trace). As suggested by Hausner et al. (2011), three reference sections of known temperature are needed to properly calibrate single-ended measurements using equation (1), as long as the differential attenuation is uniform over the section of the fiber where temperature is being measured. Any additional reference sections will provide independent zones where the calibration algorithms can be assessed using calibration metrics, as described below. Moreover, calibration algorithms should also consider the existence of step losses. Step losses consist of a signal reduction that is reflected in a sharp drop in the Raman spectra recorded by the DTS instrument (M. Hausner & Kobs, 2016; Tyler et al., 2009), thus the ratio between the Stokes and anti-Stokes intensities changes with respect to a situation without fiber damage. Hausner and Kobs (2016) present a method based on equation (1) to correct the impact of step losses on estimated temperatures, although it does not consider the effect of having fiber sections with different differential attenuation, which is common when two fibers are fused to have a duplexed cable.

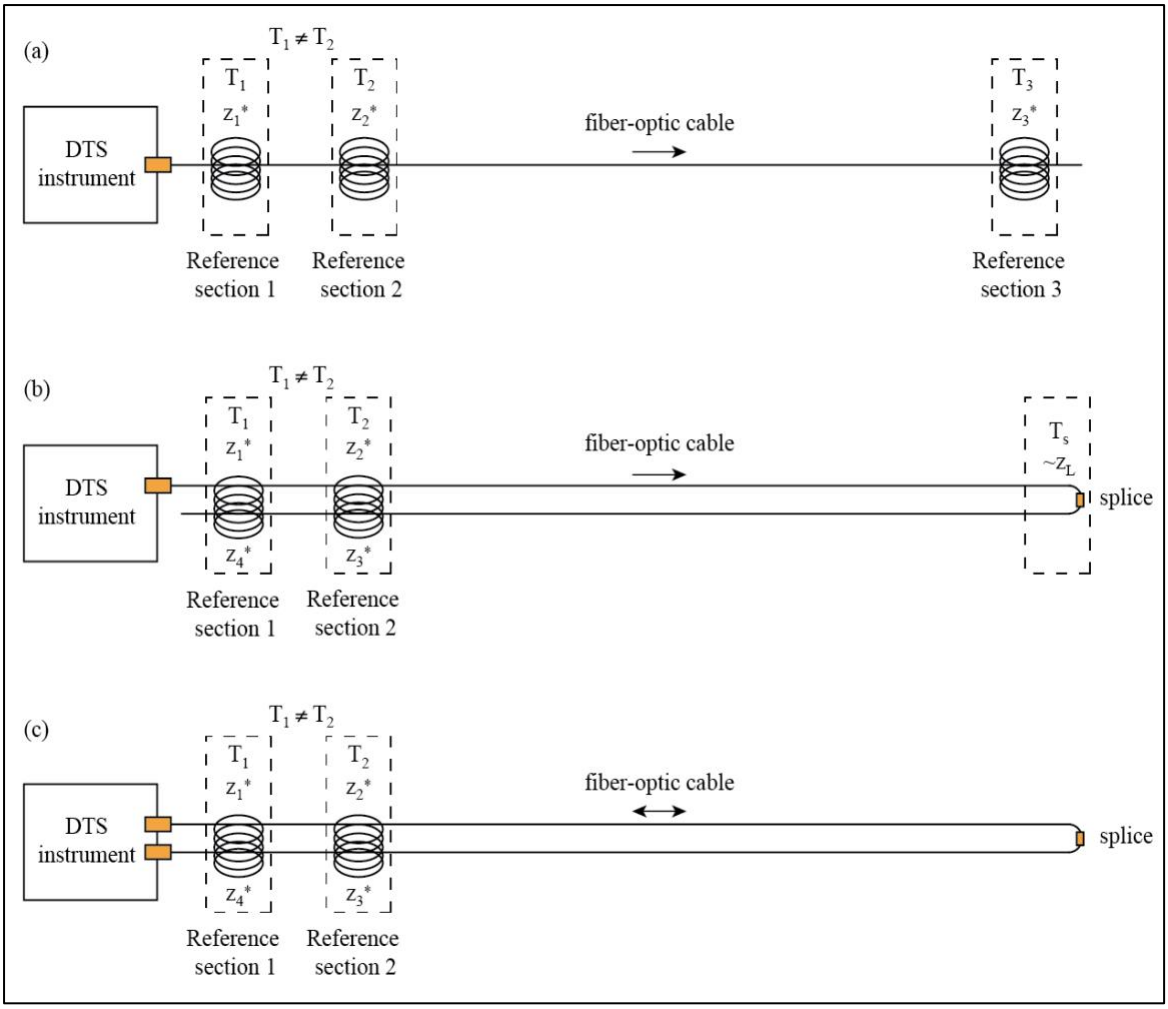

Figure 1. Typical DTS configurations. (a) Simple single-ended configuration. (b) Duplexed single-ended configuration. (c) Duplexed double-ended configuration. Modified from Hausner et al. (2011).

The general procedure to calibrate DTS temperature traces is to find the values of g, C and $\Delta\alpha$ using the data collected by the DTS combined with independent temperature measurements at known positions along the fiber, i.e., in the reference sections. For instance, Hausner et al. (2011) obtains the temperature trace using the explicit calibration method (hereafter referred to as algorithm 1) by solving a system of three equations written in matrix form:

$$\bar{A} = \begin{bmatrix} 1 & -T(z_1) & T(z_1)\, z_1 \\ 1 & -T(z_2) & T(z_2)\, z_2 \\ 1 & -T(z_3) & T(z_3)\, z_3 \end{bmatrix} \quad \vec{x} = \begin{bmatrix} \gamma \\ C \\ \Delta\alpha \end{bmatrix} \quad \vec{b} = \begin{bmatrix} T(z_1)\, R(z_1) \\ T(z_2)\, R(z_2) \\ T(z_3)\, R(z_3) \end{bmatrix}, \tag{2}$$

$$\bar{A}\vec{x} = \vec{b}\,, \tag{3}$$

where the subindices correspond to the reference sections with independent temperature measurements (see Figure 1). To obtain the best calibration, it is recommended that each reference section should have at least ten observations performed using the DTS system (M. Hausner et al., 2011; Suárez, Hausner, et al., 2011; Tyler et al., 2009). When *n* DTS observations are within a reference section, the mean distance of the reference section, $z^* = 1/n \sum_{i=1}^{n} z_i$, and the mean natural logarithm of the ratio between $I_S(z)$ and $I_{aS}(z)$, i.e., $R(z)^* = 1/n \sum_{i=1}^{n} R(z_i)$, should be used to achieve best results (M. Hausner et al., 2011).

Step losses or singularities occur frequently in field deployments due to impingements on the fiber, sharp bends or splices (M. Hausner & Kobs, 2016), and it is important to identify and remove them before performing the calibration using equations (2) and (3). Hausner and Kobs (2016) propose that step losses can be identified by visual inspection or by analyzing changes in the variance of $I_S(z)$ and $I_{aS}(z)$. Because the anti-Stokes signal is more sensitive to temperature changes compared to the Stokes signal, step losses that occur in sections with a constant temperature may result in abrupt reductions of similar magnitude in both the Stokes and anti-Stokes signal. To remove the singularities, Hausner and Kobs (2016) propose to calculate the difference of $R(z)$ at both sides of the singularity using one or more points. For instance, if the singularity is located at z_L (e.g., due to a splice, such as that shown in Figure 1 (b)), then $\Delta R = R(z_{L-1})^* - R(z_{L+1})^*$ for a section with one or more points, in which the subindices $L-1$ and $L+1$ refer to the fiber sections before and after the step loss, respectively. To correct the temperature trace, a new value of $R(z)$ must be calculated after the step loss:

$$R(z > z_L) = R(z) + \Delta R\,, \tag{4}$$

2.2. Extended calibration algorithms

Given that the previous algorithms assume a uniform differential attenuation rate throughout the fiber-optic cable for a single-ended configuration and considering that the double-ended configuration is not always feasible, we extended the current algorithms to consider two different differential attenuations in a duplexed single-ended configuration. These extensions are thought to work when the temperature at the end of the cable is unknown, and all of them also correct for step losses using the method proposed by Hausner and Kobs (2016) before applying the algorithms.

2.2.1. Calibration by sections (algorithm 2)

This algorithm is a slight modification of algorithm 1 (Hausner et al. (2011) explicit method) aimed to improve the calibration of $T(z > z_L)$. It consists of calibrating $T(z < z_L)$ using algorithm 1 and reference sections from both sides of the cable, e.g., $T(z_1^*)$, $T(z_2^*)$ and $T(z_3^*)$ (see Figure 1 (b)). From this calibration, the temperature just before z_L, $T(z_L - \Delta z)$, is used as a reference temperature in the next location after the step loss, i.e., $T(z_L - \Delta z) = T(z_L + \Delta z)$, where Δz is a distance at which the effect of the splice is not seen. Then, calibration of $T(z > z_L)$ uses algorithm 1 with the following reference locations: $T(z_L + \Delta z)$, $T(z_3^*)$ and $T(z_4^*)$. Note that this algorithm assumes that the differential attenuation of both sides of the cable is identical.

2.2.2. Explicit calibration using two differential attenuations (algorithm 3)

When a duplexed single-ended configuration is made by fusing two different fibers, it is likely that their differential attenuation will differ. Therefore, a logical and simple extension of algorithm 1 is to use $\Delta\alpha_1$ and $\Delta\alpha_2$ as the differential attenuations for the fiber before and after the step loss, respectively. In the same way than algorithm 1, a set of four equations can be written in matrix form, i.e., $\bar{A}\vec{x} = \vec{b}$, to find the calibration parameters γ, C, $\Delta\alpha_1$ and $\Delta\alpha_2$:

$$\bar{A} = \begin{bmatrix} 1 & -T(z_1) & T(z_1)\, z_1 & 0 \\ 1 & -T(z_2) & T(z_2)\, z_2 & 0 \\ 1 & -T(z_3) & T(z_3)\, z_3 & 0 \\ 1 & -T(z_4) & 0 & T(z_4)\, z_4 \end{bmatrix} \vec{x} = \begin{bmatrix} \gamma \\ C \\ \Delta\alpha_1 \\ \Delta\alpha_2 \end{bmatrix} \vec{b} = \begin{bmatrix} T(z_1)\, R(z_1) \\ T(z_2)\, R(z_2) \\ T(z_3)\, R(z_3) \\ T(z_4)\, R(z_4) \end{bmatrix} \quad (5)$$

$$T(z < z_L) = \frac{\gamma}{C + R(z) - \Delta\alpha_1\, z}, \quad (6)$$

$$T(z > z_L) = \frac{\gamma}{C + R(z) - \Delta\alpha_2\, z}, \quad (7)$$

Note that now after solving equation (3) with $\bar{A}$ and $\vec{b}$ obtained from equation (5), temperatures along the fiber are estimated using equations (6) and (7).

2.2.3. Explicit calibration using two differential attenuations and two γ (algorithm 4)

This algorithm is an extension of algorithm 3 in which γ is used as a calibration parameter that can be different before and after the step loss, i.e., now we have γ_1 and γ_2 for each side of the cable. Hence, a set of five equations can be written in matrix form to find the calibration parameters γ_1, γ_2, C, $\Delta\alpha_1$ and $\Delta\alpha_2$:

$$\bar{A} = \begin{bmatrix} 1 & 0 & -T(z_1) & \mathrm{T(z_1)\, z_1} & 0 \\ 1 & 0 & -T(z_2) & \mathrm{T(z_2)\, z_2} & 0 \\ 1 & 0 & -T(z_3) & \mathrm{T(z_3)\, z_3} & 0 \\ 0 & 1 & -\mathrm{T(z_4)} & 0 & \mathrm{T(z_4)\, z_4} \\ 0 & 1 & -\mathrm{T(z_5)} & 0 & \mathrm{T(z_5)\, z_5} \end{bmatrix} \vec{x} = \begin{bmatrix} \gamma_1 \\ \gamma_2 \\ \mathrm{C} \\ \Delta\alpha_1 \\ \Delta\alpha_2 \end{bmatrix} \vec{b} = \begin{bmatrix} T(z_1)\, R(z_1) \\ T(z_2)\, R(z_2) \\ T(z_3)\, R(z_3) \\ T(z_4)\, R(z_4) \\ T(z_5)\, R(z_5) \end{bmatrix} \quad (8)$$

$$T(z < z_L) = \frac{\gamma_1}{C + R(z) - \Delta\alpha_1\, z} \quad (9)$$

$$T(z > z_L) = \frac{\gamma_2}{C + R(z) - \Delta\alpha_2\, z} \quad (10)$$

After solving equation (3) with $\bar{A}$ and $\vec{b}$ obtained from (8), the temperatures throughout the fiber are estimated with equations (9) and (10).

2.2.4. Explicit calibration using two differential attenuations and two C (algorithm 5)

This algorithm is also an extension of algorithm 3, but in which *C* is used as a calibration parameter that can be different before and after the step loss, i.e., now we have C_1 and C_2 for each side of the cable. A set of 5 equations can be written in matrix form to find the calibration parameters γ, C_1, C_2, $\Delta\alpha_1$ and $\Delta\alpha_2$.

$$\bar{A} = \begin{bmatrix} 1 & -T(z_1) & 0 & \mathrm{T}(z_1)\, z_1 & 0 \\ 1 & -T(z_2) & 0 & \mathrm{T}(z_2)\, z_2 & 0 \\ 1 & -T(z_3) & 0 & \mathrm{T}(z_3)\, z_3 & 0 \\ 1 & 0 & -\mathrm{T}(z_4) & 0 & \mathrm{T}(z_4)\, z_4 \\ 1 & 0 & -\mathrm{T}(z_5) & 0 & \mathrm{T}(z_5)\, z_5 \end{bmatrix} \vec{x} = \begin{bmatrix} \gamma \\ C_1 \\ C_2 \\ \Delta\alpha_1 \\ \Delta\alpha_2 \end{bmatrix} \vec{b} = \begin{bmatrix} T(z_1)\, R(z_1) \\ T(z_2)\, R(z_2) \\ T(z_3)\, R(z_3) \\ T(z_4)\, R(z_4) \\ T(z_5)\, R(z_5) \end{bmatrix} \quad (11)$$

$$T(z < z_L) = \frac{\gamma}{C_1 + R(z) - \Delta\alpha_1\, z} \quad (12)$$

$$T(z > z_L) = \frac{\gamma}{C_2 + R(z) - \Delta\alpha_2\, z} \quad (13)$$

After solving equation (3) with $\bar{A}$ and $\vec{b}$ obtained from (11), the temperatures along the fiber are estimated with equations (12) and (13).

3. Materials and methods

To assess the previous calibration algorithms, we performed an experiment in the laboratory, and then we tested the algorithm that performed better with DTS data obtained in boreholes located in northern and central Chile. Below, we describe the experimental setup in the laboratory and in the different boreholes, as well as the calibration and validation metrics used to assess the calibration algorithms.

3.1. Laboratory experiment

An experiment was carried out in the Open Channel Laboratory of the Department of Hydraulic and Environmental Engineering of the Pontificia Universidad Católica de

Chile. The aim of this experiment was to replicate the deployment of a fiber-optic cable in a borehole using a duplexed single-ended configuration. Moreover, the laboratory experiment used the DTS instrument and fiber-optic cable that were used to observe the borehole in the Chilean central Andes described below.

Data were collected using a Sensornet Oryx DTS instrument (Sensornet, Hertfordshire, UK), which has two reference thermometers constructed from 100 Ω platinum PT100 sensors. These thermometers have an accuracy of 0.1 °C and a precision of 0.02 °C. The PT100 sensors were installed in two calibration baths to have reference sections with an independent temperature measurement, which is required for calibration (see Figures 2 (a) and (b)). We used a 6-mm outer diameter armored FO PBT patchcord 50/125 duplexed cable (Kaiphone Technology Co., LTD.,Taipei, Taiwan) of approximately 1.1 km. In this deployment, ~52 m of the duplexed cable passed through a recirculated water bath at ambient temperature, ~57 m of cable passed through an ice-bath that was at 0 °C, and then ~50 m of cable passed again through the ambient-temperature bath. Being a duplexed configuration, this deployment allows having up to six reference sections. Then, ~58 m of cable were lowered into one of the water reservoirs of the flumes, and after that the cable went out of the laboratory so ~117 m of cable were exposed to sun. Finally, the last ~217 m of cable were immersed in the water upstream of a weir in order to have a final section of uniform temperature due to the turbulent mixing of the water. At the end of the cable, two fibers were fused and protected allowing the duplexed single-ended configuration. Therefore, the second half of the duplexed trace must be the mirror image of the first half, but with a step loss in the middle. We installed 11 HOBO Water Temperature Pro v2 Data Loggers (Onset, Bourne, MA, USA), with an accuracy of 0.2 °C and a resolution of 0.02 °C, at different locations of the fiber to have independent temperature measurements throughout the cable: three were placed in each of the two calibration baths, two in the flume reservoir, and another three upstream of the weir (see Figure 2 (b)). Data were collected for ~6 hours using the single-ended mode with 1 m sampling interval and 2 min integration time (Table 1).

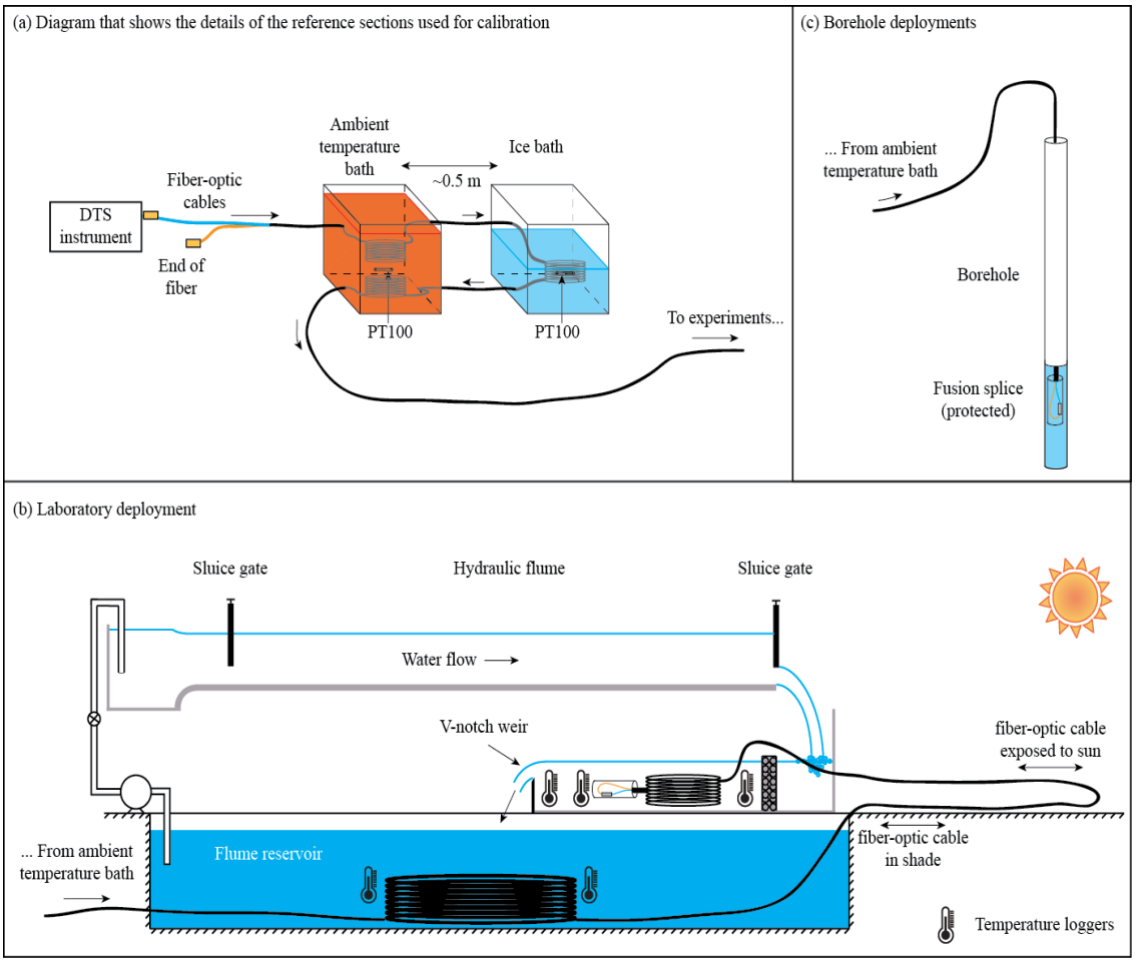

Figure 2. Laboratory and field setup (a) DTS instrument and calibration/validation sections. (b) Laboratory deployment. (c) Field deployment in boreholes (northern and central Chile experiments).

Table 1. Description of the measurements made in the laboratory and field campaigns. The Inca de Oro, Copiapó and Punta Díaz correspond to the DTS datasets collected by Pickler et al. (2018). Al the deployments have a sampling interval of 1 m and an integration time of 2 min.

Site	Coordinates	Configuration	Log ID	Observations	Traces
Laboratory		Single Ended	DIHA	2168	188
Inca de Oro	26°45’10.8’’S 69°53’38.4’’W	Single Ended	DDH2457	2187	8
		Double Ended		2187	7
Copiapó	27°22’55’’S 70°13’27’’W	Single Ended	DDH009	2187	16
		Double Ended		2187	5
Punta Diaz	28°01’56.3’’S 70°38’44.2’’W	Single Ended	RC151	2187	5
		Double Ended		2187	4
División Andina de Codelco	33°4’54’’S 70°15’18’’W	Single Ended	DAND	2168	7

3.2. Field evaluation

3.2.1. Boreholes in northern Chile: revisiting geothermal gradients using single- and double-ended data

We carried out measurements with an Ultima-XT DTS instrument (Silixa, Hertfordshire, UK) in three different boreholes located in the Atacama Desert (Inca de Oro, Copiapó, and Punta Diaz) using the proposed algorithms to obtain the associated geothermal gradient. This dataset was collected by Pickler et al. (2018) using a duplexed double-ended configuration (see Figure 1 (c)), whose fiber-optic cable passed through boreholes with depths ranging between 328 and 572 m. Therefore, the results of the proposed calibration

algorithms were compared to the double-ended measurements. Table 1 presents information related to the field site and the instrument configuration of each borehole. In these deployments, the cable was the same as that used in the laboratory experiment, with three calibration baths at the beginning of the cable, which are also seen at its end due to the duplexed nature of the cable (see Figures 2 (a) and (c)). More details about the location of the boreholes and of the collection methodology is described by Pickler et al. (2018).

3.2.2. Borehole in the Chilean central Andes: geothermal gradient

Geothermal gradient measurements were performed in a cased borehole in the División Andina (DAND) de Codelco mine, which is located more than 3,700 m ASL in the central Andes of Chile. The aim of these measurements was to observe the geothermal gradient in an unexplored region of the country, within the flat slab segment of the Nazca Plate Subduction, where no active volcanoes are present (Isacks et al., 1982). Nonetheless, given difficulties that occurred when accessing the mine, which included a damaged connector and a short time available to perform the measurements, these measurements initially had an uncertainty of ~4 °C at the far end of the fiber-optic cable, which is significant for geothermal gradient estimation.

This deployment also had the same DTS instrument, cable, and duplexed single-ended configuration as the laboratory experiment (see Figures 2 (a) and (c)). However, due to the difficulties described above, only duplexed single-ended measurements were performed with independent temperature measurements in the calibration baths. The DTS temperatures were collected with 1 m sampling interval, 1 min integration time and for ~15 min. For the analysis, the data were integrated over 2 min to be consistent with the laboratory data, as well as with the data of the boreholes located in northern Chile (Table 1).

3.3. Calibration and validation metrics

After processing the DTS data, it is important to estimate both the accuracy and precision of the calibrated data. As suggested by Hausner et al. (2011), mean bias *MB* (°C), root mean square error *RMSE* (°C), and duplexing error E_{DUP} (°C) are used as metrics for the quality of the calibration:

$$MB = \frac{1}{n}\sum_{i=1}^{n}(T_i - T)\ , \tag{14}$$

$$RMSE = \sqrt{\frac{1}{n}\sum_{i=1}^{n}(T_i - T)^2}\ , \tag{15}$$

$$E_{DUP} = \frac{1}{n}\left|\sum_{j=1}^{n} T_{j,1} - T_{j,2}\right|\ , \tag{16}$$

where T_i and T (°C) are the calibrated and independent temperatures used for calibration and/or validation, respectively; and $T_{j,1}$ and $T_{j,2}$ (°C) are the two temperature observations at the same point of the cable when using a duplexed configuration.

4. Results and Discussion

4.1. Laboratory experiment and selection of the best algorithm

A comparison of the metrics between the five algorithms, as well as the manufacturer calibration, is presented in Table 2 and 3. The calibration parameters obtained with each algorithm are presented in Table A1 (Appendix). As expected, the extended calibration algorithms outperform the manufacturer calibration. All the algorithms have a good performance in terms of *RMSE* in the calibration baths, but their accuracy decreases with distance. Temperature differences of ~1.5 °C are observed in the validation bath when using the manufacturer calibration (Figure 3). These differences are reduced to ~0.25 °C when using the extended calibration algorithms.

Algorithm 4 is the one that results in the least biased temperature and smallest *RMSE* (see validation metrics), even when algorithms 1 and 2 display better metrics in the calibration sections (see calibration metrics). Table 3 also presents the *RMSE* at the weir (see Figures

2 (b) and 3), which corresponds to the furthest location from the DTS instrument. At the weir, algorithm 4 is the one that displays best validation metrics. Data correction in a duplexed configuration is best checked by examining the duplexing error (M. Hausner et al., 2011). In the case of the laboratory calibration, the smallest duplexed error is reached with algorithm 2, followed by algorithm 4. When a second value of γ is introduced for the second half of the cable, a great improvement in terms of *RMSE*, *MB* and duplexed error is obtained (see validation metrics in Table 3). This improvement is achieved because γ, a physical parameter that should be constant, is used as a calibration parameter, in a similar way to what was carried out by Suárez et al. (2011) and Hausner et al. (2011). On the contrary, algorithm 5 presents the worst value of E_{DUP} because the algorithm overestimates the temperatures at the far end of the second section. Hence, using a different value of *C* for each side of the fiber does not improve results.

Table 2. Calibration metrics for the reference temperature baths in the laboratory deployment. The location of the calibration baths, i.e., z_1-z_6, are depicted in Figure 3.

Calibration algorithm	Calibration metrics		
	RMSE (°C) $\mu \pm \sigma$ (range)	*MB* (°C) $\mu \pm \sigma$ (range)	Calibration baths
Manufacturer calibration	0.727 ± 0.648 $(0.078\ to\ 1.375)$	-0.338 ± 0.451 $(-0.789\ to\ 0.113)$	z_1, z_2, z_5
1	0.098 ± 0.051 $(0.047\ to\ 0.150)$	-0.004 ± 0.021 $(-0.016\ to\ 0.025)$	z_1, z_2, z_5
2	0.120 ± 0.058 $(0.061 to\ 0.178)$	-0.004 ± 0.024 $(-0.028\ to\ 0.020)$	z_1, z_2, z_5, z_6
3	0.149 ± 0.103 $(0.046\ to\ 0.253)$	-0.057 ± 0.113 $(-0.170\ to\ 0.055)$	z_1, z_2, z_5, z_6
4	0.117 ± 0.058 $(0.059\ to\ 0.175)$	0.005 ± 0.003 $(0.001\ to\ 0.008)$	z_1, z_2, z_5, z_6
5	0.152 ± 0.107 $(0.044\ to\ 0.260)$	-0.060 ± 0.118 $(-0.179\ to\ 0.057)$	z_1, z_2, z_5, z_6

Table 3. Calibration metrics for the weir in the far end of the fiber and validation metrics laboratory deployment.

Calibration algorithm	Validation metrics			
	RMSE (°C) Weir $\mu \pm \sigma$ (range)	*RMSE* (°C) Validation $\mu \pm \sigma$ (range)	*MB* (°C) $\mu \pm \sigma$ (range)	E_{DUP} (°C) $\mu \pm \sigma$ (range)
Manufacturer calibration	2.171 ± 0.350 $(1.821\ to\ 2.519)$	1.579 ± 0.738 $(0.841\ to\ 2.317)$	-0.520 ± 1.642 $(-2.162\ to\ 1.121)$	0.247 ± 0.229 $(0.018\ to\ 0.476)$
1	0.454 ± 0.113 $(0.340\ to\ 0.567)$	0.332 ± 0.156 $(0.175\ to\ 0.488)$	0.078 ± 0.293 $(-0.215\ to\ 0.371)$	0.222 ± 0.166 $(0.056\ to\ 0.388)$
2	0.395 ± 0.076 $(0.319\ to\ 0.472)$	0.292 ± 0.141 $(0.151\ to\ 0.433)$	0.162 ± 0.186 $(-0.024\ to\ 0.349)$	0.156 ± 0.180 $(0\ to\ 0.336)$
3	0.488 ± 0.077 $(0.410\ to\ 0.566)$	0.347 ± 0.185 $(0.161\ to\ 0.533)$	0.218 ± 0.247 $(-0.028\ to\ 0.466)$	0.251 ± 0.232 $(0.019\ to\ 0.483)$
4	0.316 ± 0.078 $(0.238\ to\ 0.394)$	0.250 ± 0.105 $(0.144\ to\ 0.355)$	0.025 ± 0.174 $(-0.148\ to\ 0.200)$	0.192 ± 0.161 $(0.031\ to\ 0.353)$
5	0.433 ± 0.108 $(0.324\ to\ 0.541)$	0.330 ± 0.176 $(0.153\ to\ 0.507)$	0.187 ± 0.244 $(-0.057\ to\ 0.431)$	0.315 ± 0.233 $(0.081\ to\ 0.548)$

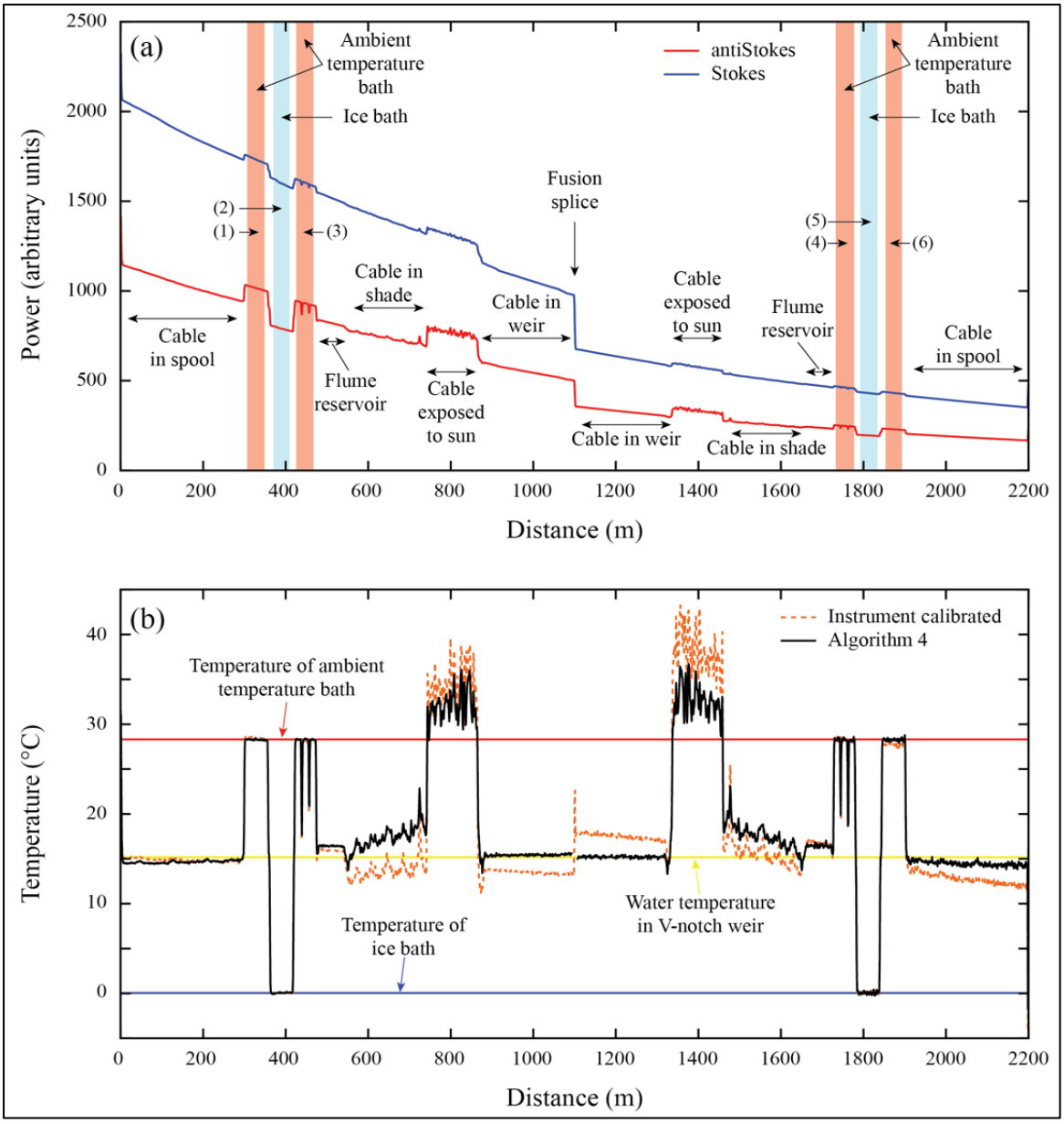

Figure 3. The laboratory deployment. (a) Raw Raman spectra data recorder by DTS and the location of the different zones along the fiber-optic cable. (b) Calibrated temperature profiles along the fiber-optic cable. The number in parenthesis in panel (a), i.e., (1)-(6), depict a reference section (calibration or validation zone).

4.2. Field evaluation

4.2.1. Boreholes in northern Chile: revisiting geothermal gradients using single- and double-ended data

Table 4 shows a comparison between the quality metrics obtained using the algorithm 4 in the northern Chile dataset, comparing the double and single-ended temperatures of each borehole (see also Figure 4). Also, Table A2 (Appendix) presents the calibration parameters obtained in each borehole. For this comparison, the comparative error (E_{COMP}) is defined as the error between single- and double-ended measurements, using the following expression:

$$E_{COMP} = \frac{1}{n}\left|\sum_{j=1}^{n} T_i^{SE} - T_i^{DE}\right|, \quad (17)$$

where T_i^{SE} and T_i^{DE} (°C) are the calibrated temperatures of the single- and double-ended measurements at the same location in the fiber.

In general, the results presented in Table 4 show a good performance of algorithm 4 compared to the double-ended temperatures in terms of *RMSE*, *MB*, E_{DUP} and E_{COMP}. This good performance is also seen in Figure 5, where the thermal profile of each borehole, obtained with single- and double-ended measurements, is presented. As shown in Table 4, Borehole DDH2457 present slightly better metrics in the calibration zones for the single-ended dataset, with all the quality metrics being less than 0.1 °C. Borehole RC151 has better quality metrics in the single-ended dataset compared to the double-ended dataset, with a difference of ~0.1 °C in the calibration zones and a similar *RMSE* in the validation zone. Furthermore, E_{COMP} of both RC151 and DDH2457 boreholes indicates a good accuracy between single- and double-ended measurements, with an average difference of 0.065 °C and 0.073 °C, respectively. The agreement between single- and double-ended measurements in borehole DDH2457 can also be observed in Figure 4. The single-ended dataset presents a higher E_{DUP} than the double-ended dataset, situation that has been improved by removing the unusual values between the environment changes, as done by Hausner et al. (2011). Finally, borehole ID DDH009 has the worst agreement

between single- and double-ended measurements, as reflected by its large E_{COMP}, although this value is still within acceptable limits.

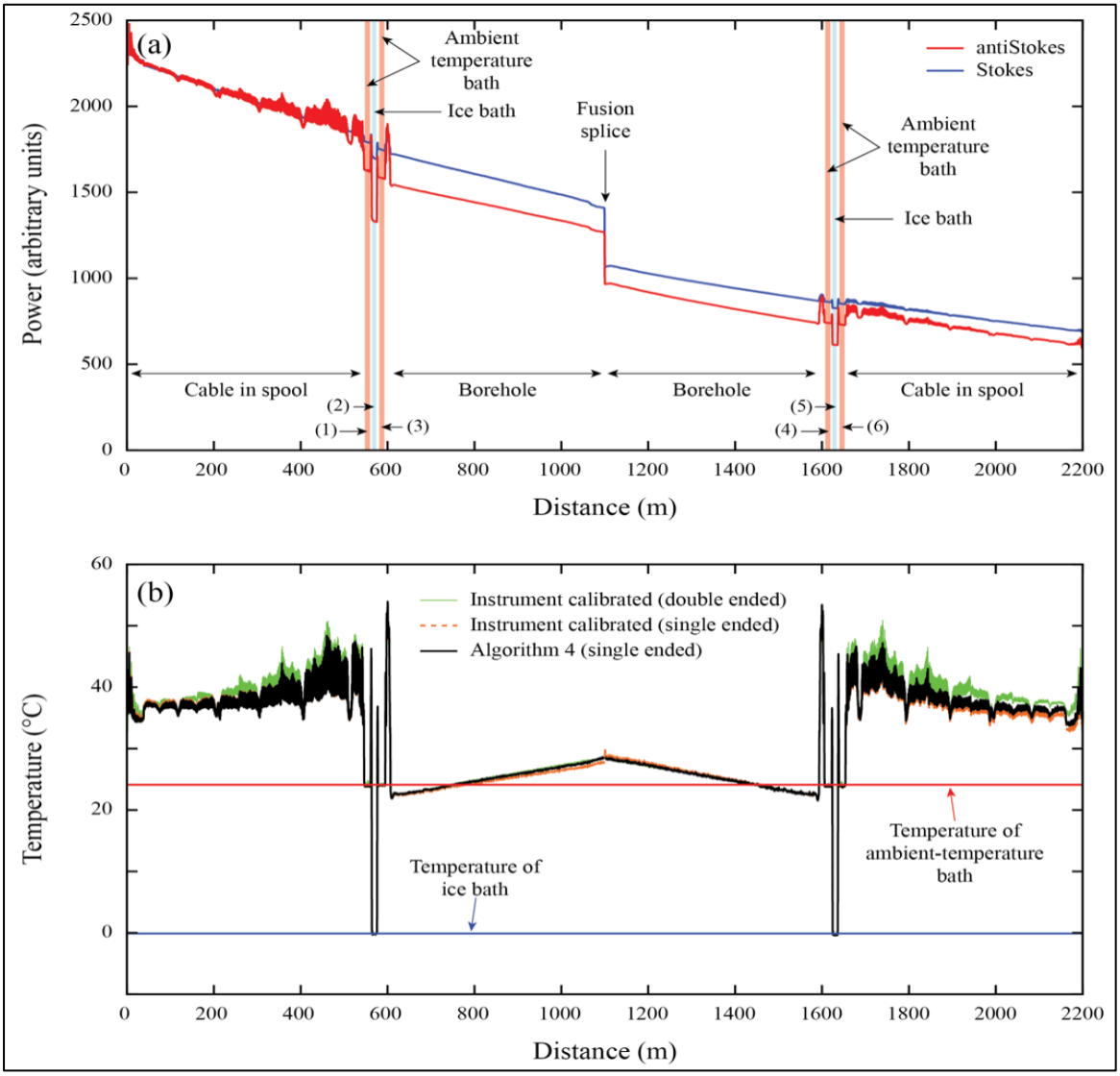

Figure 4. The northern Chile borehole deployments. As an example, borehole DDH2457 is presented: (a) Raw Raman spectra data recorded by DTS and the location of the different zones along the fiber-optic cable. (b) Calibrated temperature profiles along the fiber-optic cable. The number in parenthesis shown in panel (a), i.e., (1)-(6), depict a reference section (calibration or validation zone).

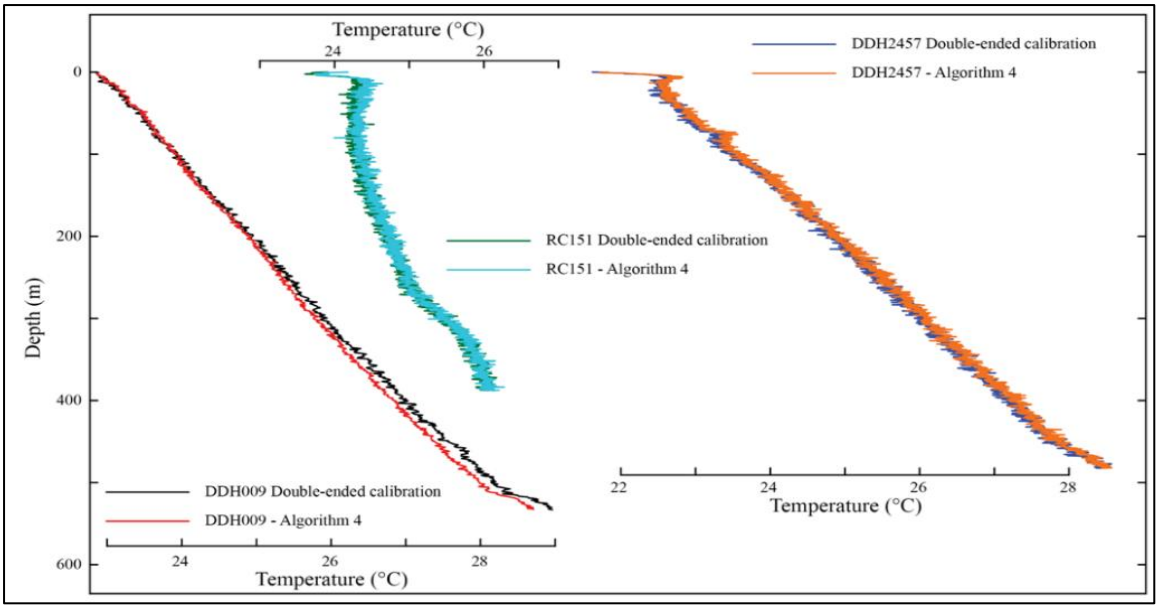

Figure 5. Geothermal profile measured in the boreholes located in northern Chile (boreholes ID DDH009, RC151 and DDH2457).

Table 4. Calibration metrics for the northern Chile data set: single-ended and double-ended calibration metrics for the RC151 borehole (calibration baths: z_1, z_2, z_5, z_6; validation baths: z_3, z_4), the DH009 borehole (calibration baths: z_1, z_2, z_3, z_4; validation baths: z_5, z_6), and the DDH2457 borehole (calibration baths: z_1, z_2 and z_4; validation baths: z_3, z_4, z_6). The position of the reference baths along the cable, i.e., z_1-z_6, are shown in Figure 4.

RC151	Single-ended measurements		Double-ended measurements	
Metric	Calibration	Validation	Calibration	Validation
RMSE (°C) $\mu \pm \sigma$ *(range)*	0.083 ± 0.019 $(0.064\ to\ 0.102)$	0.113 ± 0.021 $(0.092\ to\ 0.134)$	0.151 ± 0.068 $(0.083\ to\ 0.219)$	0.102 ± 0.010 $(0.092\ to\ 0.113)$
MB (°C) $\mu \pm \sigma$ *(range)*	0.030 ± 0.036 $(-0.005\ to\ 0.036)$	0.090 ± 0.024 $(-0.115\ to\ -0.024)$	-0.129 ± 0.082 $(-0.047\ to\ 0.211)$	-0.028 ± 0.003 $(-0.031\ to\ -0.024)$
E_{DUP} *(°C)* $\mu \pm \sigma$ *(range)*	0.512 ± 0.460 $(0.052\ to\ 0.973)$		0.494 ± 0.394 $(0.100\ to\ 0.889)$	
E_{COMP} *(°C)* $\mu \pm \sigma$ *(range)*	0.063 ± 0.047 $(0.015\ to\ 0.110)$			
DDH009	Single-ended measurements		Double-ended measurements	
Metric	Calibration	Validation	Calibration	Validation
RMSE (°C) $\mu \pm \sigma$ *(range)*	0.198 ± 0.031 $(0.166\ to\ 0.229)$	0.290 ± 0.098 $(0.192\ to\ 0.388)$	0.088 ± 0.057 $(0.031\ to\ 0.145)$	0.104 ± 0.020 $(0.084\ to\ 0.125)$
MB (°C) $\mu \pm \sigma$ *(range)*	0.032 ± 0.054 $(-0.021\ to\ 0.086)$	-0.032 ± 0.000 $(-0.021\ to\ 0.086)$	0.005 ± 0.016 $(-0.011\ to\ 0.086)$	0.096 ± 0.021 $(0.075\ to\ 0.118)$
E_{DUP} *(°C)* $\mu \pm \sigma$ *(range)*	0.445 ± 0.322 $(0.122\ to\ 0.767)$		0.324 ± 0.261 $(0.062\ to\ 0.586)$	
E_{COMP} *(°C)* $\mu \pm \sigma$ *(range)*	0.094 ± 0.101 $(0\ to\ 0.196)$			
DDH2457	Single-ended measurements		Double-ended measurements	
Metric	Calibration	Validation	Calibration	Validation
RMSE (°C) $\mu \pm \sigma$ *(range)*	0.068 ± 0.015 $(0.052\ to\ 0.084)$	0.106 ± 0.024 $(0.081\ to\ 0.130)$	0.119 ± 0.035 $(0.084\ to\ 0.153)$	0.117 ± 0.045 $(0.072\ to\ 0.163)$
MB (°C) $\mu \pm \sigma$ (range)	-0.081 ± 0.092 $(-0.011\ to\ 0.174)$	0.055 ± 0.053 $(0.005\ to\ 0.105)$	-0.047 ± 0.055 $(-0.103\ to\ 0.008)$	-0.015 ± 0.077 $(-0.092\ to\ 0.062)$
E_{DUP} *(°C)* $\mu \pm \sigma$ *(range)*	0.297 ± 0.295 $(0.001\ to\ 0.592)$		0.260 ± 0.234 $(0.025\ to\ 0.495)$	
E_{COMP} *(°C)* $\mu \pm \sigma$ *(range)*	0.073 ± 0.052 $(0.125\ to\ 0.021)$			

Table 5 presents the geothermal gradients estimated in these boreholes by Pickler et al. (2018) using the double-ended configuration, and those gradients estimated with algorithm 4 (single-ended measurements). A difference of 0.1 °C km^{-1} is obtained in borehole RC151, being the best agreement between both data sets in all these boreholes. Boreholes DDH2457 and DDH009 display a difference of 0.5 °C km^{-1} in the geothermal gradient, or approximately 5% of the estimated gradient. In all cases, the geothermal gradient estimated with single-ended measurements (algorithm 4) underestimates the geothermal gradient determined with double-ended measurements. The differences in the temperatures at the cable's end obtained with single- and double-ended configurations are less than 0.3 °C, with differences of 0.1 °C, 0.04 °C and 0.26 °C for the boreholes DDH2457, RC151 and DDH009, respectively. While for practical purposes, such as the determination of geothermal potential, the difference between the geothermal gradients is not large, temperature is one of the main geological variables and determines whether shallow temperatures are sufficient for conventional geothermal energy extraction (Vrijlandt et al., 2019). The optimal temperature depends on the intended usage of the extracted energy. For example, temperature resources less than 150 °C are used for direct heating, whereas temperatures greater than 150 °C are used for electricity generation (Sui et al., 2019). Considering a surface temperature of 20 °C and an average geothermal gradient of 10 °C km^{-1} (such as those obtained in the monitored boreholes), a difference of ~0.5 °C km^{-1} in the geothermal gradient estimation results in an uncertainty of the drilling depth of at least of 750 m to reach 150 °C. If a typical (average) geothermal gradient of 25 °C km^{-1} (DiPietro, 2013) and the same surface temperature of 20 °C are considered, the same difference of ~0.5 °C km^{-1} results in an uncertainty of ~100 m in the drilling depth to reach the same 150 °C. In contrast, considering that the errors in the geothermal gradient calculation using the BHT method could vary in 0.9 °C km^{-1}, depending on the method used for the correction of the dataset (Barba et al., 2021), an uncertainty of ~200 m in the drilling depth for an average geothermal gradient of 25 °C km^{-1}, and an uncertainty of ~1500 m for a low geothermal gradient of 10 °C km^{-1} are

obtained. Therefore, the developed algorithms allow to reduce the uncertainty in drilling depth by 50% compared with the BHT method.

Table 5. Geothermal gradients estimated in the boreholes investigated in this study.

		Single-ended measurements (algorithm 4)		Double-ended measurements	
Location	Borehole ID	Geothermal gradient (°C km^{-1})	Temperature at cable's end (°C)	Geothermal gradient (°C km^{-1})	Temperature at cable's end (°C)
Northern Chile	DDH2457	12.4	28.51	12.9	28.41
	RC151	10.4	26.09	10.5	26.05
	DDH009	9.7	28.71	10.2	28.97
Central Andes of Chile	DAND	37.8	38.71	-	-

4.2.2. Borehole in the Chilean central Andes: geothermal gradient and artesian flow estimations

Table 6 shows the metrics obtained using algorithm 4 in the Chilean central Andes dataset (DAND borehole), and Table A2 (Appendix) presents its calibration parameters. Figure 6 presents the DTS raw data, and the thermal profiles obtained with the manufacturer calibration and with algorithm 4 along the fiber-optic cable, and Figure 7 presents the temperature profile measured in the DAND borehole.

Table 6. Metrics of the central Andean Chile dataset (calibration baths: z_1, z_2, z_3, z_4; validation baths: z_5, z_6). The location of the reference baths along the fiber, i.e., z_1-z_6, are shown in Figure 6.

Metric	**Calibration**	**Validation**
RMSE (°C)	0.115 ± 0.051	0.185 ± 0.049
$\mu \pm \sigma$ (range)	$(0.064\ to\ 0.166)$	$(0.136\ to\ 0.235)$
MB (°C)	$< 10^{-4}$	0.143 ± 0.045
$\mu \pm \sigma$ (range)		$(0.097\ to\ 0.189)$
E_{DUP} (°C)	0.223 ± 0.149	
$\mu \pm \sigma$ (range)	$(0.073\ to\ 0.372)$	

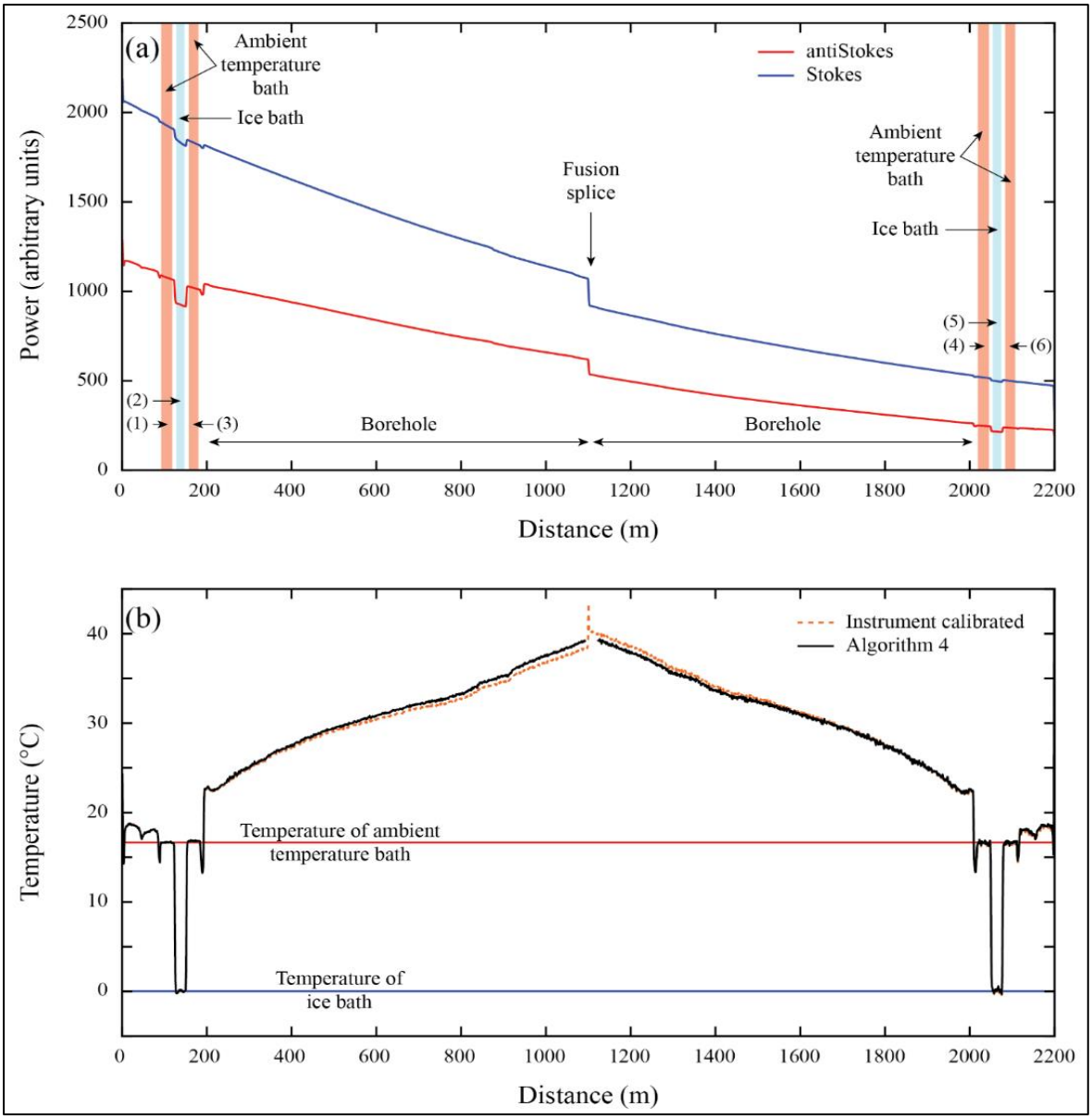

Figure 6. The central Andes deployment: (a) Raw Raman spectra data recorded by DTS and the location of the different zones along the fiber-optic cable. (b) Calibrated temperature profiles along the fiber-optic cable. The number in parenthesis shown in panel (a), i.e., (1)-(6), depict a reference section (calibration or validation zone).

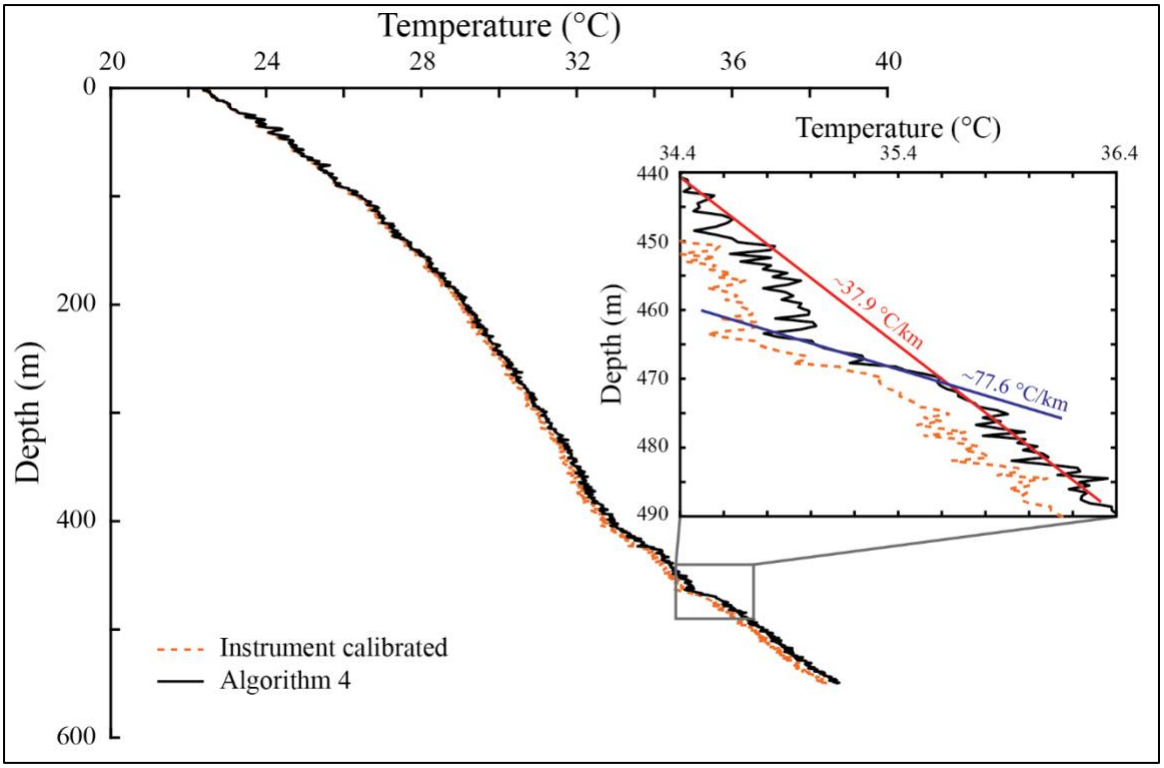

Figure 7. Geothermal profile measured in the DAND borehole located in the central Andes of Chile.

In the validation section, *RMSE* and *MB* are lower than 0.2 °C, whereas the duplexed error is slightly larger (0.22 °C). The *RMSE* in the validation section is smaller than that obtained in the laboratory setup (Table 2) and in the DDH009 borehole (Table 4), but larger than those obtained in RC151 and DDH2457 boreholes (Table 4). The *MB* is smaller than that obtained in the laboratory deployment (Table 2 and 3), but larger than those of the other boreholes (Table 4). Nonetheless, all these errors are much lower than those obtained with the typical calibration algorithms: an uncertainty in the estimated temperature at the cable's end of 4 °C in the DAND borehole was estimated with the different algorithms developed previously. Considering the deployment made in the laboratory, it is possible to improve the temperature estimation in the far-end of the cable using the proposed algorithm 4. This improvement could not be achieved without

performing the independent laboratory experiment, which had a similar deployment configuration than that of the DAND borehole.

In the DAND borehole, after correcting for the dip, we estimated a geothermal gradient of ~37.9 °C km^{-1}. This geothermal gradient was determined using the temperature data from the last 170 m of cable, which exhibited a linear trend. The vertical distance of the last 170 m of cable are equivalent to 105 m in the vertical direction, as the borehole was inclined. This geothermal gradient is consistent with the normal (average) geothermal gradient of the Earth's surface in a normal crust within the first 3 km and away from volcanic sources (the nature of the flat slab segment in which this borehole was located) (DiPietro, 2013). Valdenegro et al. (2019) reported a borehole gradient of 20 °C km^{-1}, but their work assumed the borehole was vertical and did not correct for the drilling dip. However, a larger thermal gradient in the area is in better agreement with Valdenegro et al. (2019) model at this region (above 25 °C km^{-1}).

At ~460-480 m depth, cool water flowing through a confined aquifer was detected (see zoom in Figure 7). This water did not enter the borehole as it was cased but perturbed the geothermal profile. This cool-water aquifer locally increased the geothermal profile up to ~77.6 °C km^{-1}, which cannot be explained by changes in the thermal properties of the rock, as the borehole was drilled in Granodiorite that has a relatively uniform thermal conductivity of ~1.8 W m^{-1} K^{-1} (Suárez et al., 2014). The water input that entered at the bottom of the cased borehole flows upward, emerging through the upper part of the well, modifying the temperature profile at shallow depths, in which a parabolic shape is observed (Figure 7).

The significance of the improvement in the determination of the temperature at the cable's end can also be explained using the example presented in the previous section, in which one would like to find the depth where a temperature of 150 °C occurs to define the borehole depth required for electricity generation. In the DAND borehole, the temperature at ~500 m depth is of ~37.9 °C (Figure 7). Assuming an error of ~4 °C in that temperature,

and a geothermal gradient of ~37.9 °C km^{-1}, the depth where 150 °C is achieved is ~3 km, and the uncertainty in this depth is of ~100 m. This uncertainty is reduced to ~10 m when the error in the temperature at the end of the cable is of ~0.2 °C. Moreover, if the geothermal gradient in the DAND borehole has an uncertainty of ~0.1 °C km^{-1}, errors of ~4 and 0.2°C in the estimation of the temperature at the cable's end results in uncertainties of ~120 and ~25 m, respectively, for the depths required to achieve the 150 °C. Therefore, this method provides a reliable tool to obtain geothermal gradient with confidence, so implementation of new algorithms to improve DTS temperature estimations are important and must be considered in any field deployment.

4.3. Limitations of the proposed extended algorithms

As demonstrated above, the proposed extended DTS calibration algorithms greatly improve the accuracy and precision of thermal measurements along the fiber-optic cable when no temperature information is available at the end of the cables. Nonetheless, these algorithms have limitations that must be considered when they are applied.

The main limitation is related to the assumption of having a uniform differential attenuation at each section of the cables. Even when the proposed algorithms consider that the two fibers co-located in a single cable can have different differential attenuation between each other, they are unable to improve the thermal measurements along fibers that have spatially distributed differential attenuations. For such situations, double-ended configurations are the most appropriate approach to calibrate DTS temperatures as the fibers are interrogated from both sides and, consequently, differential attenuation can be resolved at every segment of the fiber (van de Giesen et al., 2012). This situation cannot be successfully resolved using single-ended data, unless step losses are the solely reason of observing unexpected variations in the raw data. In this case, it is critical to remove the step losses using the approach developed by Hausner and Kobs (2016) before applying the methods proposed in this research.

The second limitation is associated to the fact that some of the parameters used in the calibration process not necessarily fulfill physical considerations, hence, physical parameters are converted into calibration parameters. For instance, most of the algorithms uses γ as a calibration parameter instead of being the shift in energy between a photon at the wavelength of the incident laser and the scattered Raman photon. Nonetheless, this issue also applies to previous developed methods (M. Hausner et al., 2011).

Regarding limitations related to the deployment itself, the proposed calibration algorithms require at least four reference baths with at least two different temperatures. As this research is focused on duplexed single-ended configurations, this is not a significant issue as these reference sections will be located near the DTS instrument.

5. Conclusions

Geothermal exploration requires obtaining accurate measurements at the bottom of boreholes, especially if a certain temperature must be reached in the drilling to exploit the geothermal resource. An accurate measurement will significantly reduce the existing uncertainty related to the rock temperature at a given depth. Our results show that the uncertainty in drilling can be reduced by 50% when using DTS methods (compared to the BHT approach).

Calibrated single- and double-ended temperature data in the northern Chile boreholes had similar results at the far end of the cable, with differences of up to 0.3 °C. Although the double-ended configuration is preferable, as it does not require to know the temperature at the end of the cable, the developed algorithms reduced the uncertainty compared to the already existing algorithms in cases when double-ended are not possible.

Different fiber optic DTS calibration algorithms, including the manufacturer calibration, have a good performance in the first meters of cable considering the calibration and validation zones, but an analysis of the last meters of the cable (> 1000 m) determine that the temperature difference is even 2.5 °C. Considering only existing and proposed algorithms, it is possible to improve accuracy up to 0.25 °C in the cable's last meters. This

improvement is possible when calibration regions are located in both sections of the fiber. Moreover, a further reduction of the calibration uncertainty can be achieved when an independent temperature measurement is available at the end of the fiber.

Future work should investigate new extensions of the algorithms for other DTS configurations and determining the flow rate of the DAND artesian well using the geothermal profile provided by the DTS measurements and the available data of the borehole.

6. Appendix

Tables A1 and A2 present the parameters used to estimate the thermal profile along the fiber-optic cable using the different algorithms in the laboratory deployment and in the boreholes measured.

Table A 1 Calibration parameters obtained in the laboratory deployment. Reported values correspond to the mean ± standard deviation.

Algorithm	C_1 (-) (range)	C_2 (-) (range)	γ_1 (K) (range)	γ_2 (K) (range)	$\Delta\alpha_1 \times 10^{-5}$ (m^{-1}) (range)	$\Delta\alpha_2 \times 10^{-5}$ (m^{-1}) (range)
1	1.083 ± 0.002 (1.081 to 1.086)	–	483.2 ± 0.4 (482.8 to 483.6)	–	8.007 ± 0.048 (7.959 to 8.055)	–
2	1.083 ± 0.002 (1.081 to 1.086)	1.075 ± 0.003 (1.072 to 1.078)	483.2 ± 0.4 (482.8 to 483.6)	479.6 ± 0.7 (478.9 to 480.2)	8.007 ± 0.048 (7.959 to 8.055)	8.269 ± 0.066 (8.203 to 8.335)
3	1.083 ± 0.002 (1.081 to 1.086)	–	483.0 ± 0.4 (482.6 to 483.4)	–	8.098 ± 0.047 (8.053 to 8.143)	8.027 ± 0.046 (7.980 to 8.073)
4	1.083 ± 0.002 (1.081 to 1.086)	–	483.2 ± 0.4 (482.8 to 483.6)	480.2 ± 0.5 (479.6 to 480.7)	8.007 ± 0.048 (7.959 to 8.055)	8.616 ± 0.153 (8.511 to 8.772)
5	1.083 ± 0.002 (1.081 to 1.086)	1.084 ± 0.002 (1.081 to 1.086)	483.2 ± 0.4 (482.8 to 483.6)	–	8.007 ± 0.048 (7.959 to 8.147)	8.102 ± 0.048 (8.057 to 8.147)

Table A 2. Calibration parameters obtained in the borehole deployments for algorithm 4. Reported values correspond to the mean ± standard deviation.

Borehole	C (-) (range)	γ_1 (K) (range)	γ_2 (K) (range)	$\Delta\alpha_1 \times 10^{-5}$ (m^{-1}) (range)	$\Delta\alpha_2 \times 10^{-5}$ (m^{-1}) (range)
DDH2457	1.542 ± 0.006 (1.536 to 1.548)	484.2 ± 0.4 (483.9 to 484.6)	484.0 ± 0.4 (483.6 to 484.5)	5.847 ± 0.059 (5.788 to 5.906)	5.896 ± 0.057 (5.838 to 5.953)
RC151	1.623 ± 0.018 (1.605 to 1.642)	496.3 ± 2.5 (493.8 to 498.9)	496.6 ± 2.4 (494.3 to 499.0)	5.639 ± 0.079 (5.560 to 5.718)	5.566 ± 0183 (5.383 to 5.750)
DDH009	1.576 ± 0.021 (1.555 to 1.597)	489.2 ± 1.5 (487.7 to 490.6)	489.0 ± 1.5 (487.5 to 490.6)	5.612 ± 0.159 (5.453 to 5.771)	5.642 ± 0.161 (5.481 to 5.803)
DAND	1.061 ± 0.007 (1.054 to 1.068)	474.0 ± 2.2 (471.8 to 476.2)	473.7 ± 2.2 (471.5 to 475.9)	8.414 ± 0.033 (8.381 to 8.447)	8.506 ± 0.037 (8.469 to 8.544)

REFERENCES

Araya Vargas, J., Sanhueza, J., & Yáñez, G. (2021). The Role of Temperature in the Along-Margin Distribution of Volcanism and Seismicity in Subduction Zones: Insights From 3-D Thermomechanical Modeling of the Central Andean Margin. *Tectonics, 40*(11), e2021TC006879. https://doi.org/10.1029/2021TC006879

Arnon, A., Selker, J., & Lensky, N. (2014). Correcting artifacts in transition to a wound optic fiber: Example from high-resolution temperature profiling in the Dead Sea. *Water Resources Research*, *50*(6), 5329-5333. https://doi.org/10.1002/2013WR014910

Barba, D. paul, Barragán, R., Gallardo, J., & Salguero, A. (2021). Geothermal Gradients in the Upper Amazon Basin derived from BHT data. *International Journal of Terrestrial Heat Flow and Applied Geothermics*, *4*(1), 85-94. https://doi.org/10.31214/ijthfa.v4i1.58

Beltrami, H., & Mareschal, J.-C. (1992). Ground temperature histories for central and eastern Canada from geothermal measurements: Little Ice Age signature. *Geophysical Research Letters*, *19*(7), 689-692. https://doi.org/10.1029/92GL00671

Bense, V. F., Read, T., Bour, O., Borgne, T. L., Coleman, T., Krause, S., Chalari, A., Mondanos, M., Ciocca, F., & Selker, J. S. (2016). Distributed Temperature Sensing as a downhole tool in hydrogeology. *Water Resources Research*, *52*(12), 9259-9273. https://doi.org/10.1002/2016WR018869

Cande, S. C., Leslie, R. B., Parra, J. C., & Hobart, M. (1987). Interaction between the Chile Ridge and Chile Trench: Geophysical and geothermal evidence. *Journal of Geophysical Research*, *92*, 495-520. https://doi.org/10.1029/JB092iB01p00495

Clauser, C., & Mareschal, J.-C. (1995). Ground temperature history in central Europe from borehole temperature data. *Geophysical Journal International*, *121*(3), 805-817. https://doi.org/10.1111/j.1365-246X.1995.tb06440.x

Dai, G., Fan, X., & He, Z. (2018). A Long-range Fiber-optic Raman Distributed Temperature Sensor Based on Dual-source Scheme and RZ Simplex Coding. *2018 Asia*

Communications and Photonics Conference (ACP), 1-3. https://doi.org/10.1109/ACP.2018.8596150

Dhia, H. B. (1987). The geothermal gradient map of Central Tunisia: Comparison with structural, gravimetric and petroleum data. *Tectonophysics*, *142*(1), 99-109. https://doi.org/10.1016/0040-1951(87)90297-6

DiPietro, J. A. (2013). Keys to the Interpretation of Geological History. En *Landscape Evolution in the United States* (pp. 327-344). Elsevier. https://doi.org/10.1016/B978-0-12-397799-1.00020-8

Domra Kana, J., Djongyang, N., Danwe Raïdandi, Njandjock Nouck, P., & Abdouramani Dadjé. (2015). A review of geophysical methods for geothermal exploration. *Renewable and Sustainable Energy Reviews*, *44*, 87-95. https://doi.org/10.1016/j.rser.2014.12.026

Drury, M. J. (1984). On a possible source of error in extracting equilibrium formation temperatures from borehole BHT data. *Geothermics*, *13*(3), 175-180. https://doi.org/10.1016/0375-6505(84)90014-2

Förster, A., Schrötter, J., Merriam, D. F., & Blackwell, D. D. (1997). Application of optical-fiber temperature logging—An example in a sedimentary environment. *GEOPHYSICS*, *62*(4), 1107-1113. https://doi.org/10.1190/1.1444211

Ghafoori, Y., Vidmar, A., Říha, J., & Kryžanowski, A. (2020). A Review of Measurement Calibration and Interpretation for Seepage Monitoring by Optical Fiber Distributed Temperature Sensors. *Sensors*, *20*(19), 5696. https://doi.org/10.3390/s20195696

Goutorbe, B., Lucazeau, F., & Bonneville, A. (2007). Comparison of several BHT correction methods: A case study on an Australian data set. *Geophysical Journal International*, *170*(2), 913-922. https://doi.org/10.1111/j.1365-246X.2007.03403.x

Gupta, H., & Roy, S. (2007). EXPLORATION TECHNIQUES. En *Geothermal Energy* (pp. 61-119). Elsevier. https://doi.org/10.1016/B978-044452875-9/50005-8

Hausner, M. B., Wilson, K. P., Gaines, D. B., Suárez, F., & Tyler, S. W. (2013). The

shallow thermal regime of Devils Hole, Death Valley National Park: The shallow shelf of Devils Hole. *Limnology and Oceanography: Fluids and Environments*, *3*(1), 119-138. https://doi.org/10.1215/21573689-2372805

Hausner, M., & Kobs, S. (2016). Identifying and Correcting Step Losses in Single-Ended Fiber-Optic Distributed Temperature Sensing Data. *Journal of Sensors*, *in press*. https://doi.org/10.1155/2016/7073619

Hausner, M., Suárez, F., Glander, K., van de Giesen, N., Selker, J., & Tyler, S. (2011). Calibrating Single-Ended Fiber-Optic Raman Spectra Distributed Temperature Sensing Data. *Sensors (Basel, Switzerland)*, *11*, 10859-10879. https://doi.org/10.3390/s111110859

Hurtig, E., Großwig, S., Jobmann, M., Kühn, K., & Marschall, P. (1994). Fibre-optic temperature measurements in shallow boreholes: Experimental application for fluid logging. *Geothermics*, *23*(4), 355-364. https://doi.org/10.1016/0375-6505(94)90030-2

Isacks, B., Jordan, T., Allmendinger, R., & Ramos, V. (1982). *La segmentación tectónica de los Andes centrales y su relación con la geometría de la placa de Nazca subductada*. *3*, 587-606. https://biblioteca.sernageomin.cl/opac/index.asp?param=o%AD%88%92bi%98%8Dof&Op=3

Iwamori, H. (2000). Thermal effects of ridge subduction and its implications for the origin of granitic batholith and paired metamorphic belts. *Earth and Planetary Science Letters*, *181*(1-2), 131-144. https://doi.org/10.1016/S0012-821X(00)00182-5

Kutasov, I. M., & Eppelbaum, L. V. (2009). *Estimation of geothermal gradients from single temperature log-field cases*. 131-135.

Lagos, M., Serna, J. L., Muñoz, J. F., & Suárez, F. (2020). Challenges in determining soil moisture and evaporation fluxes using distributed temperature sensing methods. *Journal of Environmental Management*, *261*, 110232.

https://doi.org/10.1016/j.jenvman.2020.110232

Li, H., Liu, Q., Chen, D., & He, Z. (2021). Centimeter Spatial Resolution Distributed Temperature Sensor Based on Polarization-Sensitive Optical Frequency Domain Reflectometry. *Journal of Lightwave Technology*, *39*(8), 2594-2602. https://doi.org/10.1109/JLT.2021.3052036

Li, J., Li, J., Zhang, Q., Zhang, Q., Xu, Y., Xu, Y., Zhang, M., Zhang, M., Zhang, J., Zhang, J., Qiao, L., Qiao, L., Promi, M. M., Promi, M. M., Wang, T., & Wang, T. (2019). High-accuracy distributed temperature measurement using difference sensitive-temperature compensation for Raman-based optical fiber sensing. *Optics Express*, *27*(25), 36183-36196. https://doi.org/10.1364/OE.27.036183

Liu, C., Li, K., Chen, Y., Jia, L., & Ma, D. (2016). Static Formation Temperature Prediction Based on Bottom Hole Temperature. *Energies*, *9*(8), 646. https://doi.org/10.3390/en9080646

Lowell, R. P., Kolandaivelu, K., & Rona, P. A. (2014). Hydrothermal Activity☆. En *Reference Module in Earth Systems and Environmental Sciences* (p. B9780124095489092000). Elsevier. https://doi.org/10.1016/B978-0-12-409548-9.09132-6

Lowry, C. S., Walker, J. F., Hunt, R. J., & Anderson, M. P. (2007). Identifying spatial variability of groundwater discharge in a wetland stream using a distributed temperature sensor. *Water Resources Research*, *43*(10). https://doi.org/10.1029/2007WR006145

Lv, S., Zeng, Y., Wen, J., Zhao, H., & Su, Z. (2018). Estimation of Penetration Depth from Soil Effective Temperature in Microwave Radiometry. *Remote Sensing*, *10*(4), 519. https://doi.org/10.3390/rs10040519

Macenić, M., Kurevija, T., & Medved, I. (2020). Novel geothermal gradient map of the Croatian part of the Pannonian Basin System based on data interpretation from 154 deep exploration wells. *Renewable and Sustainable Energy Reviews*, *132*, 110069.

https://doi.org/10.1016/j.rser.2020.110069

Madon, M., & Jong, J. (2021). Geothermal gradient and heat flow maps of offshore Malaysia: Some updates and observations. *Bulletin of the Geological Society of Malaysia*, *71*, 159-183. https://doi.org/10.7186/bgsm71202114

Miranda, M. M., Raymond, J., & Dezayes, C. (2020). Uncertainty and Risk Evaluation of Deep Geothermal Energy Source for Heat Production and Electricity Generation in Remote Northern Regions. *Energies (19961073)*, *13*(16), 4221. Academic Search Ultimate.

Morata, D. (2014). ¿Chile: Un país geotérmico en un futuro inmediato? *Anales de la Universidad de Chile*, *5*, 73-86.

Muñoz, M., & Hamza, V. (1993). Heat flow and temperature gradients in Chile. *Studia Geophysica et Geodaetica*, *37*, 315-348. https://doi.org/10.1007/BF01624604

Nian, Y.-L., & Cheng, W.-L. (2018). Evaluation of geothermal heating from abandoned oil wells. *Energy*, *142*, 592-607. https://doi.org/10.1016/j.energy.2017.10.062

Ovnatanov, S. T., & Tamrazyan, G. P. (1970). Thermal Studies in Subsurface Structural Investigations, Apsheron Peninsula, Azerbaijan, USSR1. *AAPG Bulletin*, *54*(9), 1677-1685. https://doi.org/10.1306/5D25CBDD-16C1-11D7-8645000102C1865D

Peters, K., & Nelson, P. (2012). Criteria to Determine Borehole Formation Temperatures for Calibration of Basin and Petroleum System Models. En *SEPM Special Publication* (Vol. 103, pp. 5-15). https://doi.org/10.2110/sepmsp.103.005

Pickler, C., Gurza Fausto, E., Beltrami, H., Mareschal, J.-C., Suárez, F., Chacon-Oecklers, A., Blin, N., Cortés Calderón, M. T., Montenegro, A., Harris, R., & Tassara, A. (2018). Recent climate variations in Chile: Constraints from borehole temperature profiles. *Climate of the Past*, *14*(4), 559-575. https://doi.org/10.5194/cp-14-559-2018

Ruskowitz, J. A., Suárez, F., Tyler, S. W., & Childress, A. E. (2014). Evaporation suppression and solar energy collection in a salt-gradient solar pond. *Solar Energy*, *99*,

36-46. https://doi.org/10.1016/j.solener.2013.10.035

Sayde, C., Thomas, C. K., Wagner, J., & Selker, J. (2015). High-resolution wind speed measurements using actively heated fiber optics. *Geophysical Research Letters*, *42*(22), 10,064-10,073. https://doi.org/10.1002/2015GL066729

Selker, J. S., Thévenaz, L., Huwald, H., Mallet, A., Luxemburg, W., Giesen, N. van de, Stejskal, M., Zeman, J., Westhoff, M., & Parlange, M. B. (2006). Distributed fiber-optic temperature sensing for hydrologic systems. *Water Resources Research*, *42*(12). https://doi.org/10.1029/2006WR005326

Sellwood, S., Hart, D., & Bahr, J. (2015). An in-well heat-tracer-test method for evaluating borehole flow conditions. *Hydrogeology Journal*, *23*. https://doi.org/10.1007/s10040-015-1304-8

Steele-Dunne, S., Rutten, M., Krzeminska, D., Hausner, M., Tyler, S., Selker, J., Bogaard, T., & van de Giesen, N. (2010). Feasibility of soil moisture estimation using passive distributed temperature sensing. *Water Resour. Res*, *46*. https://doi.org/10.1029/2009WR008272

Suárez, F., Aravena, J., Hausner, M., Childress, A., & Tyler, S. (2011). Assessment of a vertical high-resolution distributed-temperature-sensing system in a shallow thermohaline environment. *Hydrology and Earth System Sciences*, *15*. https://doi.org/10.5194/hess-15-1081-2011

Suárez, F., Childress, A. E., & Tyler, S. W. (2010). Temperature evolution of an experimental salt-gradient solar pond. *Journal of Water and Climate Change*, *1*(4), 246-250. https://doi.org/10.2166/wcc.2010.101

Suárez, F., Hausner, M., Dozier, J., Selker, J., & Tyler, S. (2011). *Heat Transfer in the Environment: Development and Use of Fiber-Optic Distributed Temperature Sensing*. https://doi.org/10.5772/19474

Suárez, F., Lobos, F., de la Fuente, A., Vilà-Guerau de Arellano, J., Prieto, A., Meruane,

C., & Hartogensis, O. (2020). E-DATA: A Comprehensive Field Campaign to Investigate Evaporation Enhanced by Advection in the Hyper-Arid Altiplano. *Water*, *12*(3), 745. https://doi.org/10.3390/w12030745

Suárez, F., Sotomayor, R., Oportus, T., Yáñez, G., Hausner, M. B., & Muñoz, M. (2014). Complementando el conocimiento hidrogeológico mediante sistemas distribuidos de temperatura. *Congreso Latinoamericano de hidrogeología*, *12*, 9.

Sui, D., Wiktorski, E., Røksland, M., & Basmoen, T. A. (2019). Review and investigations on geothermal energy extraction from abandoned petroleum wells. *Journal of Petroleum Exploration and Production Technology*, *9*(2), 1135-1147. https://doi.org/10.1007/s13202-018-0535-3

Tyler, S. W., Holland, D. M., Zagorodnov, V., Stern, A. A., Sladek, C., Kobs, S., White, S., Suárez, F., & Bryenton, J. (2013). Using distributed temperature sensors to monitor an Antarctic ice shelf and sub-ice-shelf cavity. *Journal of Glaciology*, *59*(215), 583-591. https://doi.org/10.3189/2013JoG12J207

Tyler, S. W., Selker, J. S., Hausner, M. B., Hatch, C. E., Torgersen, T., Thodal, C. E., & Schladow, S. G. (2009). Environmental temperature sensing using Raman spectra DTS fiber-optic methods. *Water Resources Research*, *45*(4). https://doi.org/10.1029/2008WR007052

Valdenegro, P., Muñoz, M., Yáñez, G., Parada, M. A., & Morata Céspedes, D. (2019). A model for thermal gradient and heat flow in central Chile: The role of thermal properties. *Journal of South American Earth Sciences*. https://doi.org/10.1016/j.jsames.2019.01.011

van de Giesen, N., Steele-Dunne, S. C., Jansen, J., Hoes, O., Hausner, M. B., Tyler, S., & Selker, J. (2012). Double-Ended Calibration of Fiber-Optic Raman Spectra Distributed Temperature Sensing Data. *Sensors (Basel, Switzerland)*, *12*(5), 5471-5485. https://doi.org/10.3390/s120505471

van Ramshorst, J. G. V., Coenders-Gerrits, M., Schilperoort, B., van de Wiel, B. J. H.,

Izett, J. G., Selker, J. S., Higgins, C. W., Savenije, H. H. G., & van de Giesen, N. C. (2019). *Wind speed measurements using distributed fiber optics: A windtunnel study* [Preprint]. Others (Wind, Precipitation, Temperature, etc.)/Laboratory Measurement/Instruments and Platforms. https://doi.org/10.5194/amt-2019-63

Vrijlandt, M., Struijk, M., Brunner, L., Veldkamp, J. G., Witmans, N., Maljers, D., & Van Wees, J. (2019). *ThermoGIS update: A renewed view on geothermal potential in the Netherlands*. 11-14.

Watson, K., Kruse, F. A., & Hummer-Miller, S. (1990). Thermal infrared exploration in the Carlin trend, northern Nevada. *GEOPHYSICS, 55*(1), 70-79. https://doi.org/10.1190/1.1442773

Williams, G., Brown, G., Hartog, A., & Waite, P. (2000). Distributed temperature sensing (DTS) to characterize the performance of producing oil wells. *Proceedings of SPIE - The International Society for Optical Engineering*, *4202*. https://doi.org/10.1117/12.411726